Chapter 1
Surface and Interface Physics: Its Definition and Importance

A solid interface is defined as a small number of atomic layers that separate two solids in intimate contact with one another, where the properties differ significantly from those of the bulk material it separates. A metal film deposited on a semiconductor crystal, for example, is thus separated by the semiconductor–metal interface from the bulk of the semiconductor.

The surface of a solid is a particularly simple type of interface, at which the solid is in contact with the surrounding world, i.e., the atmosphere or, in the ideal case, the vacuum. The development of modern interface and thin film physics is thus basically determined by the theoretical concepts and the experimental tools being developed in the field of surface physics, i.e., the physics of the simple solid–vacuum interface. Surface physics itself has mean-while become an important branch of microscopic solid-state physics, even though its historical roots lie both in classical bulk solid-state physics and physical chemistry, in particular the study of surface reactions and heterogeneous catalysis.

Solid-state physics is conceptually an atomic physics of the condensed state of matter. According to the strength of chemical bonding, the relevant energy scale is that between zero and a couple of electron volts. The main goal consists of deriving an atomistic description of the macroscopic properties of a solid, such as elasticity, specific heat, electrical conductance, optical response or magnetism. The characteristic difference from atomic physics stems from the necessity to describe a vast number of atoms, an assembly of about 10^{23} atoms being contained in 1 cm^3 of condensed matter; or the 10^8 atoms that lie along a line of 1 cm in a solid. In order to make such a large number of atoms accessible to a theoretical description, new concepts had to be developed in bulk solid-state physics. The translational symmetry of an ideal crystalline solid leads to the existence of phonon dispersion branches or the electronic band structure and the effective mass of an electron. Because of the large number of atoms involved, and because of the difference between the macroscopic and the atomic length scale, most theoretical models in classic solid-state theory are based on the assumption of an infinitely extended solid. Thus, in these models, the properties of the relatively small number of atoms forming the surface of the macroscopic solid are neglected. This simplifies the mathematical description

H. Lüth, *Solid Surfaces, Interfaces and Thin Films*, Graduate Texts in Physics,
DOI 10.1007/978-3-319-10756-1_1

considerably. The infinite translational symmetry of the idealized crystalline solid allows the application of a number of symmetry operations, which makes a handy mathematical treatment possible. This description of the solid in terms of an infinitely extended object, which neglects the properties of the few different atomic layers at the surface, is a good approximation for deriving macroscopic properties that depend on the total number of atoms contained in this solid. Furthermore, this description holds for all kinds of spectroscopic experiments, where the probes (X-rays, neutrons, fast electrons, etc.) penetrate deep into the solid material and where the effect of the relatively few surface atoms ($\approx 10^{15}$ cm^{-2}) can be neglected.

The approach of classical solid-state physics in terms of an infinitely extended solid becomes highly questionable and incorrect, however, when probes are used which "strongly" interact with solid matter and thus penetrate only a couple of Ångstroms into the solid, such as low-energy electrons, atomic and molecular beams, etc. Here the properties of surface atoms, being different from those of bulk atoms, become important. The same is true for spectroscopies where the particles detected outside the surface originate from excitation processes close to the surface. In photoemission experiments, for example, electrons from occupied electronic states in the solid are excited by X-rays or UV light; they escape into the vacuum through the surface and are analyzed and detected by an electron spectrometer. Due to the very limited penetration depth of these photoelectrons (5–80 Å depending on their energy) the effect of the topmost atomic layers below the surface cannot be neglected. The photoelectron spectra carry information specific to these topmost atomic layers. Characteristic properties of the surface enter the theoretical description of a photoemission experiment (Panel XII: Chap. 6). Even when bulk electronic states are studied, the analysis of the data is done within the framework of models developed in surface physics. Furthermore, in order to get information about intrinsic properties of the particular solid, the experiment has to be performed under Ultra-High Vacuum (UHV) conditions on a freshly prepared clean sample surface. Because of the surface sensitivity, the slightest contamination on the surface would modify the results.

The concepts of surface and interface physics are important in solid-state physics not only in connection with special experimental tools, but also for certain physical systems. A thin solid film deposited on a substrate is bounded by a solid–solid interface and by its surface (film–vacuum interface). The properties of such a thin film are thus basically determined by the properties of its two interfaces. Thin-film physics cannot be reduced to the concepts of bulk solid-state physics, but instead the models of interface physics have to be applied. Similarly, the physics of small atomic clusters, which often possess more surface than "bulk" atoms, must take into account the results from surface physics.

Surface and interface physics, as a well-defined sub-discipline of general condensed-matter physics, is thus interrelated in a complex way with a number of other research fields (Fig. 1.1). This is particularly true if one considers the input from other domains of physics and chemistry and the output into important fields of application such as semiconductor electronics and the development of new experimental equipment and methods. The scheme in Fig. 1.1 emphasizes

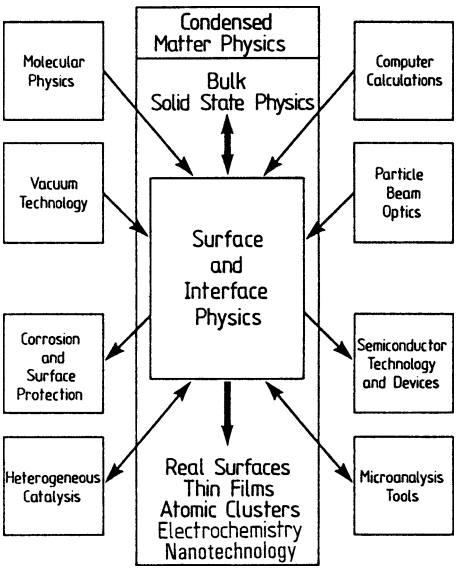

Fig. 1.1 Interrelation of surface and interface physics as a subdiscipline of condensed-matter physics with other research fields

the way in which surface and interface physics is embedded in the general field of condensed-matter physics, as well as the strong impact of the models of bulk solid-state physics (phonon dispersion, electronic bands, transport mechanisms, etc.) on the concepts of interface physics.

On the other hand, within general solid-state physics, interface physics provides a deeper understanding of the particular problems related to the real surfaces of a solid and to thin films, dealing with both their physical properties and their growth mechanisms. The physics of small atomic clusters also benefits from surface physics, as does the wide field of electro-chemistry, where the reaction of solid surfaces with an ambient electrolyte is the central topic. Furthermore, the new branch of nanotechnology, i.e. engineering on a nanometer scale (Panel VI: Chap. 3), which has emerged as a consequence of the application of scanning tunneling microscopy and related techniques, uses concepts that have largely been developed in surface sciences.

Modern surface and interface physics would not have been possible without the use of results from research fields other than bulk solid-state physics. From the experimental viewpoint, the preparation of well-defined, clean surfaces, on which surface studies are usually performed, became possible only after the development of UHV techniques. Vacuum physics and technology had a strong impact on surface and thin film physics. Surface sensitive spectroscopies use particles (low-energy electrons, atoms, molecules, etc.) because of their "strong" interaction with matter, and thus the development of particle beam optics, spectrometers and detectors is intimately related to the advent of modern surface physics. Since adsorption processes on solid surfaces are a central topic in surface physics, not only the properties of the solid substrate but also the physics of the adsorbing molecule is an ingredient in the understanding of the complex adsorption process. The physics and chemistry of molecules also plays an essential role in many questions in surface physics. Last,

but not least, modern surface and interface physics would never have reached the present level of theoretical understanding without the possibility of large and complex computer calculations. Many calculations are much more extensive and tedious than in classical bulk solid-state physics since, even for a crystalline solid, a surface or interface breaks the translational symmetry and thus considerably increases the number of equations to be treated (loss of symmetry).

From the viewpoint of applications, surface and interface physics can be considered as the basic science for a number of engineering branches and advanced technologies. A better understanding of corrosion processes, and thus also the development of surface protection methods, can only be expected on the basis of surface studies. Modern semiconductor device technology would be quite unthinkable without research on semiconductor surfaces and interfaces. With an increasing trend towards greater miniaturization (large-scale integration) surfaces and interfaces become an increasingly important factor in the functioning of a device. Furthermore, the preparation techniques for complex multilayer devices and nanostructures—Molecular Beam Epitaxy (MBE), metal organic MBE (Chap. 2)—are largely derived from surface-science techniques. In this field, surface science research has led to the development of new technologies for semiconductor-layer preparation and nanostructure research.

An interdependence between surface physics and applied catalysis research can also be observed. Surface science has contributed much to a deeper atomistic understanding of important adsorption and reaction mechanisms of molecules on catalytically active surfaces, even though practical heterogeneous catalysis occurs under temperature and pressure conditions totally different from those on a clean solid surface in a UHV vessel. On the other hand, the large amount of knowledge derived from classical catalysis studies under less well-defined conditions has also influenced surface science research on well-defined model systems. A similar interdependence exists between surface physics and the general field of applied microanalysis. The demand for extremely surface-sensitive probes in surface and interface physics has had an enormous impact on the development and improvement of new particle spectroscopies. Auger Electron Spectroscopy (AES), Secondary Ion Mass Spectroscopy (SIMS) and High-Resolution Electron Energy Loss Spectroscopy (HREELS) are good examples. These techniques were developed within the field of surface and interface physics [1.1]. Meanwhile they have become standard techniques in many other fields of practical research, where microanalysis is required.

Surface and interface physics thus has an enormous impact on other fields of research and technology. Together with the wide variety of experimental techniques being used in this field, and with the input from various other branches of chemistry and physics, it is a truly interdisciplinary field of physical research [1.2–1.14].

Characteristic for this branch of physics is the intimate relation between experimental and theoretical research, and the application of a wide variety of differing experimental techniques having their origin sometimes in completely different fields. Correspondingly, this text follows a concept, where the general theoretical framework of surface and interface physics, as it appears at present, is treated in

parallel with the major experimental methods described in so-called panels. In spite of the diversity of the experimental methods and approaches applied so far in this field, there is one basic technique which seems to be common to all modern surface, interface and thin film experiments: UHV equipment is required to establish clean conditions for the preparation of a well-defined solid surface or the performance of in situ studies on a freshly prepared interface. If one enters a laboratory for surface or interface studies, large UHV vessels with corresponding pumping stations are always to be found. Similarly, the importance of particle-beam optics and analytical tools, in particular for low-energy electrons, derives from the necessity to have surface sensitive probes available to establish the crystallographic perfection and cleanliness of a freshly prepared surface.

Panel I
Ultrahigh Vacuum (UHV) Technology

From the experimental point of view, the development of modern surface and interface physics is intimately related to the advent of UltraHigh Vacuum (UHV) techniques. The preparation of well-defined surfaces with negligible contamination requires ambient pressures lower than 10^{-10} Torr ($= 10^{-10}$ mbar or approximately 10^{-8} Pa) (Sect. 2.1). Typical modern UHV equipment consists of a stainless-steel vessel, the UHV chamber, in which the surface studies or processes (epitaxy, sputtering, evaporation, etc.) are performed, the pumping station including several different pumps, and pressure gauges covering different pressure ranges. In many cases a mass spectrometer (usually a Quadrupole Mass Spectrometer, QMS, Panel IV: Chap. 2) is also attached to the main vessel in order to monitor the residual gas. Figure I.1 shows a schematic view over the whole set-up. A combination of different pumps is necessary in order to obtain background pressures in the main UHV chamber on the order of 10^{-10} Torr, since each pump can only operate over a limited pressure range. The UHV range (lower than 10^{-9} Torr) is covered by diffusion and turbomolecular pumps, and also by ion and cryopumps (Fig. I.2). Starting pressures for diffusion, ion, and cryopumps are in the 10^{-2}–10^{-4} Torr range, i.e. rotary or sorption pumps are needed to establish such a pressure in the main vessel (e.g., using a bypass line as in Fig. I.1). A turbomolecular pump can be started at atmospheric pressure in the UHV chamber and can operate down into the UHV regime, but a rotary pump is then needed as a backing pump (Fig. I.1). Valves are used to separate the different pumps from one another and from the UHV chamber, since a pump that has reached its operating pressure, e.g. 10^{-3} Torr for a rotary pump, acts as a leak for other pumps operating down to lower pressures.

An important step in achieving UHV conditions in the main vessel is the bake-out process. When the inner walls of the UHV chamber are exposed to air, they become covered with a water film (H_2O sticks well due to its high dipole moment). On pumping down the chamber, these H_2O molecules would slowly desorb and, despite the high pumping power, 10^{-8} Torr would be the lowest pressure obtainable. In order to get rid of this water film the whole equipment has to be baked in vacuum for about 10 h at a temperature of 150–180 °C. When a pressure of about 10^{-7} Torr is reached in the chamber the bake-out oven (dashed line in Fig. I.1) is switched on.

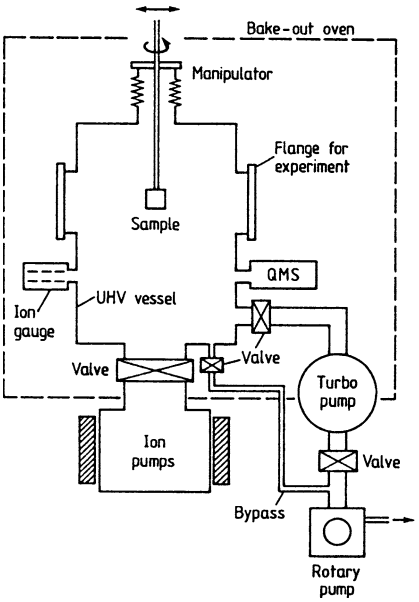

Fig. I.1 Schematic view of an Ultrahigh High Vacuum (UHV) system: stainless steel UHV vessel pumped by different pumps; the rotary backing pump can be connected to the main chamber in order to establish an initial vacuum before starting the ion pumps. Quadrupole mass spectrometer (QMS) and ion gauge are used for monitoring the residual gas. All parts enclosed by the *dashed line* (bake-out oven) must be baked in order to achieve UHV conditions

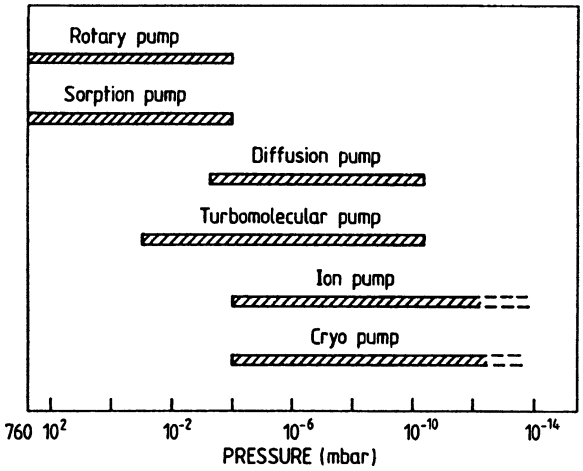

Fig. I.2 Pressure ranges in which different types of pumps can be employed

After switching off the bake-out equipment, again at $\approx 10^{-7}$ Torr the pressure falls down into the UHV regime.

After this rough overview of the whole system, the main parts of the equipment will now be described in somewhat more detail. The different parts of a UHV system are joined together by standard flange systems. Apart from minor modifications the so-called *conflat flange* (in different standard sizes: miniconflat, 2 2/3″, 4″, 6″, 8″, etc.) is used by all UHV suppliers (Fig. I.3). Sealing is achieved by a copper gasket which, to avoid leaks, should only be used once. This conflat-flange system is necessary for all bakeable parts of the equipment. Backing pumps, bypass

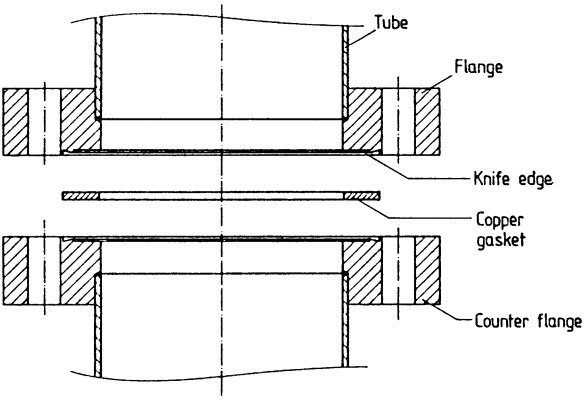

Fig. I.3 Cross section through a stainless steel Conflat flange which is used in UHV equipment for sealing

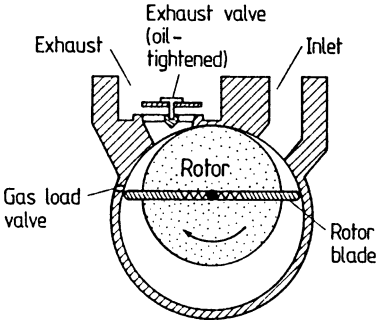

Fig. I.4 Schematic cross section through a rotary roughing pump. During the gas inlet phase the inlet volume expands. Further rotation of the eccentric rotor causes compression of this volume until the outlet phase is reached

lines, and other components not under UHV, are usually connected by rubber or viton fittings.

In order to establish an initial vacuum (10^{-2}–10^{-3} Torr) prior to starting a UHV pump, sorption pumps or rotary pumps are used. This procedure is known as *roughing out the system* and such pumps often go by the corresponding name of *roughing* pumps.

A *sorption pump* contains pulverized material (e.g., zeolite) with a large active surface area, the so-called *molecular sieve*, which acts as an adsorbant for the gas to be pumped. The maximum sorption activity, i.e. the full pumping speed, is reached at low temperature. The sorption pump is thus activated by cooling its walls with liquid nitrogen. From time to time regeneration of the sorbant material is necessary by means of heating under vacuum. Since the sorption process will saturate sooner or later, the sorption pump cannot be used continuously.

In combination with turbomolecular pumps, one thus uses *rotary pumps* to obtain the necessary backing pressure (Fig. I.4). The rotary pump functions on the basis of changing gas volumes produced by the rotation of an eccentric rotor, which has two blades in a diametrical slot. During the gas inlet phase, the open volume near the inlet expands, until, after further rotation, this volume is separated from the inlet. Then, during the compression phase, the gas is compressed and forced through the exhaust valve (oil tightened). In order to avoid the condensation of vapor contained

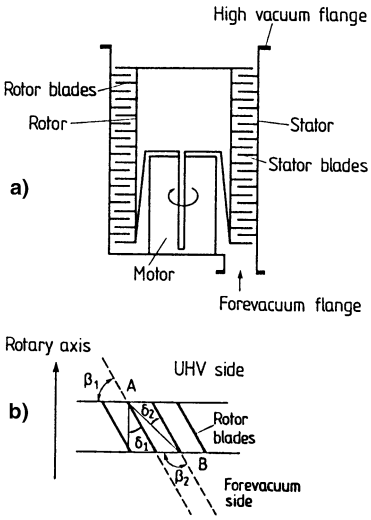

Fig. I.5 Schematic representation of a turbomolecular pump (**a**) general arrangement of rotor and stator. Rotor and stator blades (not shown in detail) are inclined with respect to one another. (**b**) Qualitative view of the arrangement of the rotor blades with respect to the axis of rotation. The possible paths of molecules from the UHV side to the backing side and vice versa are geometrically determined by the angles β_1, δ_1, and β_2, δ_2, respectively

in the pumped air, most pumps are supplied with a gas load valve, through which a certain amount of air, the gas load is added to the compressed gas. Sealing between rotary blades and inner pump walls is performed by an oil film.

The pumps that are regularly used in the UHV regime are the turbo-molecular pump, the diffusion pump, the ion pump and the cryopump.

The principle of the *turbomolecular pump* (or turbopump) rests on the action of a high-speed rotor (15 000–30 000 rpm) which "shuffles" gas molecules from the UHV side to the backing side, where they are pumped away by a rotary pump (Fig. I.5). The rotor, which turns through, and is interleaved with, the so-called *stator*, has "shuffling" blades, which are inclined with respect to the rotation axis (as are the inversely inclined stator blades). This means that the probability of a molecule penetrating the rotor from the backing side to the UHV side is much lower than that of a molecule moving in the reverse direction. This becomes clear if one considers the possible paths of molecules moving through the assembly of rotor blades (Fig. I.5(b)). A molecule hitting the rotor blade at point A (least favorable case) can, in principle, pass from the UHV side to the backing side, if it impinges at an angle of at most β_1 and leaves within δ_1. For a molecule to pass through the rotor in the opposite direction, it must impinge within an angular range β_2 and leave within δ_2 in the least favorable case in which it arrives at point B. The probabilities of these two paths can be estimated from the ratios of angles δ_1/β_1 and δ_2/β_2. Since δ_2/β_2 is considerably smaller than δ_1/β_1, the path from the UHV side outwards is favored and pumping action occurs. This purely geometric pumping effect is strongly enhanced by the high blade velocity. Because of the blade inclination, molecules hitting the blade gain a high velocity component away from the UHV region. Compression is further enhanced by the presence of the stator blades with their reverse inclination. A molecule moving in the "right" direction always finds its way open into the backing line.

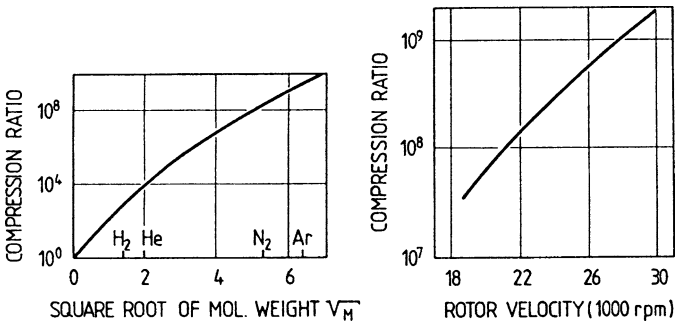

Fig. I.6 Compression ratio of a turbomolecular pump as a function of molecular weight M of the molecules pumped (*left*) and of the rotor velocity (*right*). (After Leybold Heraeus GmbH)

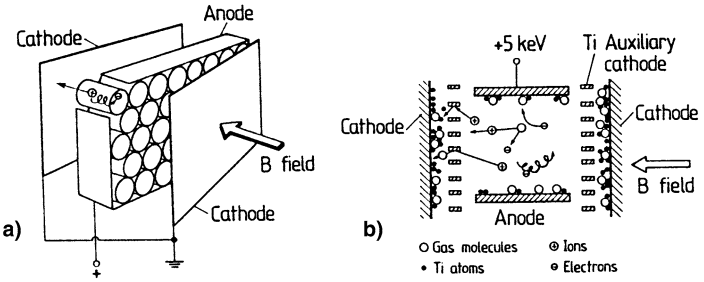

Fig. I.7 (**a**), (**b**) Schematic view of an ion-getter pump: (**a**) The basic multicell arrangement. Each cell consists essentially of a tube-like anode. The cells are sandwiched between two common cathode plates of Ti, possibly together with auxiliary cathodes of Ti. (**b**) Detailed representation of the processes occurring within a single cell. Residual gas molecules are hit by electrons spiralling around the magnetic field B and are ionized. The ions are accelerated to the cathode and/or auxiliary cathode; they are trapped on the active cathode surface or they sputter Ti atoms from the auxiliary cathode, which in turn help to trap further residual gas ions

Since the pumping action of a turbomolecular pump relies on impact processes between the pumped molecules and the rotor blades, the compression ratio between backing and UHV sides depends on the molecular mass of the gases and on the rotor velocity (Fig. I.6). A disadvantage of turbomolecular pumps is thus their low pumping speed for light gases, in particular for H_2 (Fig. I.6, left). An important advantage is the purely mechanical interaction of the gas molecules with the pump; no undesirable chemical reactions occur. Turbopumps are employed mainly when relatively large quantities of gas have to be pumped out, e.g., during evaporation or epitaxy (MOMBE).

Ion-getter pumps, which have no rotating parts, are very convenient as standby pumps for maintaining UHV conditions for an extended period (Fig. I.7). Modern ion-getter pumps are designed as multicell pumps (Fig. I.7(a)), in which the pumping speed is enhanced by simple repetition of the action of a single pump element (Fig. I.7(b)). Within each element an electrical discharge is produced between the

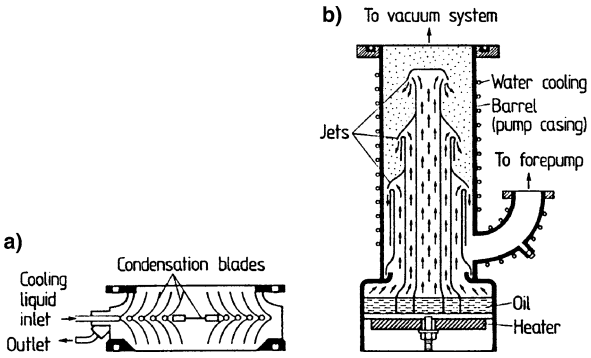

Fig. I.8 Simplified representation of a vapor (diffusion) pump (**b**) together with a baffle or cold trap (**a**) on the high vacuum side. Baffle (**a**) and pump (**b**) are arranged one on top of the other in a pumping station

anode and the cathode at a potential of several thousand volts and in a magnetic field of a few thousand Gauss (produced by permanent magnets outside the pump). Since the magnetic field causes the electrons to follow a helical path, the length of their path is greatly increased. A high efficiency of ion formation down to pressures of 10^{-12} Torr and less is assured by this long path length. The ions so-formed are accelerated to the Ti cathode, where they are either captured or chemisorbed. Due to their high energies they penetrate into the cathode material and sputter Ti atoms, which settle on the surfaces of the anode where they also trap gas atoms. To enhance the pumping speeds, auxiliary cathodes are used (triode pump, Fig. I.7(b)). One problem with ion pumps is caused by Ar, which is usually the determining factor for the pumping speed (the atmosphere contains 1 % Ar). This problem can be tackled to some extent by using auxiliary cathodes. Sputter ion pumps are available with a wide range of pumping speeds, between 1 ℓ/s and 5000 ℓ/s. The pressure range covered is 10^{-4} to less than 10^{-12} Torr; thus a backing pump is needed to start an ion-getter pump. Ion-getter pumps should not be used in studies of adsorption processes and surface chemistry with larger molecules, since cracking of the background gas molecules might occur, thereby inducing additional unwanted reactions.

In those cases, *vapor pumps* are a convenient alternative. The general term *vapor pump* includes both ejector pumps and diffusion pumps. In both types of pump, a vapor stream is produced by a heater at the base of the pump (Fig. I.8(b)). The vapor, oil or mercury, travels up a column (or a combination of several columns) and reaches an umbrella-like deflector placed at the top. There the vapor molecules collide with the gas molecules entering through the intake part. When the mean-free path of the gas molecules is greater than the throat width, the interaction between gas and vapor is based on diffusion, which is responsible for dragging the gas molecules towards the backing region. Thus diffusion induces the pressure gradient between the UHV and backing sides. When the mean free path of the gas molecules at the intake is less than the clearance, the pump acts as an ejector pump. The gas is entrained by viscous drag and turbulent mixing, and is carried down the pump chamber and through an orifice near the backing side. In some modern types of vapor pumps, combinations of the diffusion and ejector principles are used; these pumps are called

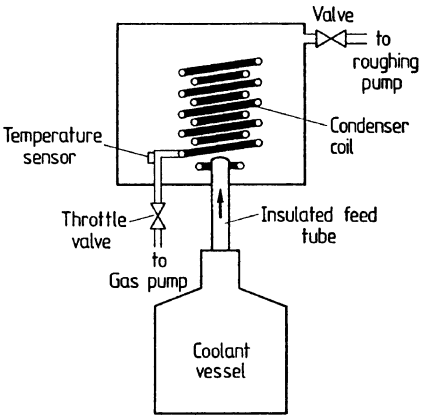

Fig. I.9 Schematic diagram of a cryopump. (After Leybold Heraeus GmbH)

vapor booster pumps. Diffusion pumps suffer from two drawbacks that limit their final pressure. Back-streaming and back-migration of molecules of the working fluid give rise to particle migration in the wrong direction. The vapor pressure of the working fluid is thus important for the finally obtainable pressure. The same is true for molecules of the pumped gas which can also back-diffuse to the high vacuum side. Both effects can be reduced by using baffles and cold traps, which obviously lower the net pumping speed but are necessary to reach UHV conditions. The baffles contain liquid-nitrogen cooled blades, on which the back-streaming species condense (Fig. I.8(a)). The consistency of the working fluid is thus very important for the performance of vapor pumps. Mercury, which was in exclusive use in former times, has now been largely displaced by high-quality ultrahigh vacuum oils, which enable pressures in the 10^{-10} Torr range to be reached when cooling traps are used.

Because of their extremely high pumping speeds *cryopumps* are gaining popularity for large UHV systems. Cryogenic pumping is based on the fact that if a surface within a vacuum system is cooled, vapor (gas molecules) tends to condense upon it, thus reducing the ambient pressure. A typical cryopump is sketched in Fig. I.9. The main part is a metallic helix which serves as the condenser surface. It is mounted in a chamber that is directly flanged to the UHV vessel to be evacuated. The coolant, usually liquid helium, is supplied from a dewar to the helix through a vacuum-insulated feed tube. It is made to flow through the coil by means of a gas pump at the outlet end of the helix. The coolant boils as it passes through the coil, hence cooling the tube. A throttle valve in the gas exhaust line controls the flux and thus the cooling rate. A temperature sensor fixed to the coil automatically controls the valve setting. Closed-loop systems are also in use; here, the pump coil is directly connected to a helium liquifier and a compressor. The helium gas from the exhaust is fed back into the liquifier.

A second type of cryopump is the so-called *bath pump*, whose coolant is contained in a tank which must be refilled from time to time. The ultimate pressure $p_{\min}$ of such a cryopump for a given gas is determined by the vapor pressure P_v at the temperature T_v of the condenser surface. According to Fig. I.10 most gases, except He and H_2, are effectively pumped using liquid He as a coolant (4.2 K) such

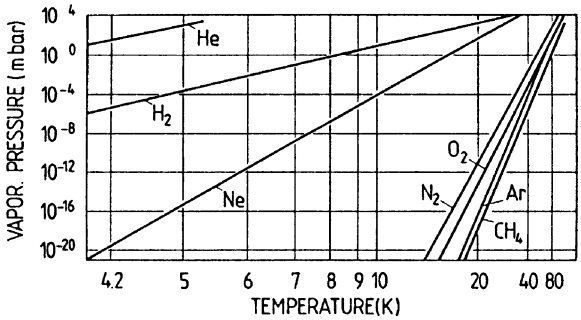

Fig. I.10 Saturation vapor pressures of various coolant materials as a function of temperature

that pressures below 10^{-10} Torr are easily obtained. Extremely high pumping speeds of between 10^4 and 10^6 ℓ/s are achieved. Cryopumps cannot be used at pressures above 10^{-4} Torr, partly because of the large quantities of coolant that would be required, and partly because thick layers of deposited solid coolant would seriously reduce the pump efficiency.

The most important aspect of UHV technology is of course the generation of UHV conditions. However, a further vital requirement is the ability to measure and constantly monitor the pressure. In common with pumps, pressure gauges can also operate only over limited pressure ranges. The entire regime from atmospheric pressure down to 10^{-10} Torr is actually covered by two main types of manometer. In the higher-pressure regime, above 10^{-4} Torr, *diaphragm gauges* are used. The pressure is measured as a volume change with respect to a fixed gas volume by the deflection of a (metal) diaphragm or bellow. The reading is amplified optically or electrically, e.g. by a capacitance measurement (capacitance gauge). A further type of gauge that can operate in the high-pressure range is the molecular *viscosity gauge*. Since the viscosity of a gas is a direct function of its pressure, the measurement of the decay of a macroscopic motion induced by molecular drag can be used to determine the pressure. Even pressures as low as 10^{-10} Torr can be measured by spinning-ball manometers. In this equipment a magnetically suspended metal ball rotates at high speed and its deceleration due to gas friction is measured, also magnetically.

Very commonly used in vacuum systems are *thermal conductivity* (*heat loss*) *gauges*, which can be used from about 10^{-3} up to about 100 Torr. These manometers rely on the pressure dependence of the thermal conductivity of a gas as the basis for the pressure measurement. The essential construction consists of a filament (Pt or W) in a metal or glass tube attached to the vacuum system. The filament is heated directly by an electric current. The temperature of the filament then depends on the rate of supply of electrical energy, the heat loss due to conduction through the surrounding gas, the heat loss due to radiation and the heat loss by conduction through the support leads. The losses due to radiation via the support leads can be minimized by suitable construction. If the rate of supply of electrical energy is constant, then the temperature of the wire and thus also its resistance depend primarily on the loss of energy due to the thermal conductivity of the gas. In the so-called *Pirani gauge*, the temperature variations of the filament with pressure are measured in terms of the change in its resistance. This resistance measurement is usually per-

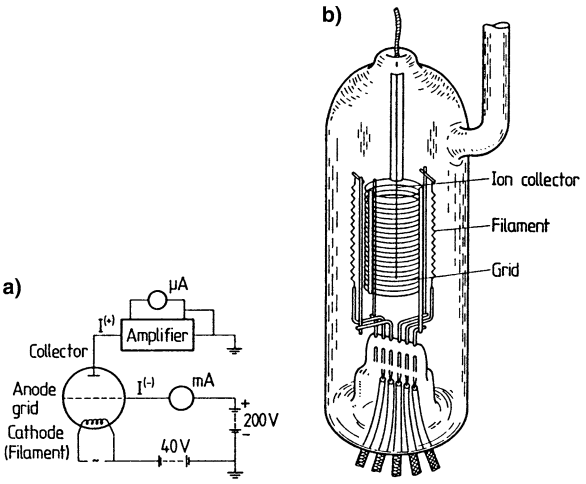

Fig. I.11 (**a**), (**b**) Ionization gauge for pressure monitoring between 10^{-4} and 10^{-10} Torr. (**a**) Electric circuit for measuring the electron emission current I^- and the ion (collector) current I^+. (**b**) Typical construction of a modern Bayard–Alpert type ionization gauge. Cathode filament, anode grid and ion collector are contained in a glass (pyrex) tube which is attached to the UHV chamber. The electrode arrangement can also be put directly into the UHV chamber

formed with a Wheatstone bridge, in which one leg of the bridge is the filament of the gauge tube. The measured resistance versus pressure dependence is, of course, nonlinear. Calibration against other absolute manometers is necessary.

The most important device for measuring pressures lower than 10^{-4} Torr, i.e., including the UHV range ($<10^{-10}$ Torr), is the *ionization gauge*. Residual gas atoms exposed to an electron beam of sufficient kinetic energy (12.6 eV for H_2O and O_2; 15–15.6 eV for N_2, H_2, Ar; 24.6 eV for He) are subject to ionization. The ionization rate and thus the ion current produced are a direct function of the gas pressure. Hot-cathode ionization gauges as in Fig. I.11 consist essentially of an electrically heated cathode filament (+40 V), an anode grid (+200 V) and an ion collector. The thermally emitted electrons are accelerated by the anode potential and ionize gas atoms or molecules on their path to the anode. The electron current I^- is measured at the anode, whereas the ion current, which is directly related to the ambient pressure, is recorded as the collector current I^+. In operation as a pressure gauge the electron emission current I^- is usually kept fixed, such that only I^+ needs to be recorded in order to determine the pressure. Since the ionization cross section is specific to a particular gas, a calibration against absolute standards is necessary and correction factors for each type of residual gas molecule have to be taken into account. Commercially available instruments are usually equipped with a pressure scale appropriate for N_2. Modern, so-called *Bayard–Alpert gauges* are constructed as in Fig. I.11(b), with several filaments (as spares), a cylindrical grid structure and a fine wire as ion collector in the center of the tube. Only this particular construction with a very thin ion collector enables pressure measurements below 10^{-8} Torr (UHV range). Spatially more extended ion collectors give rise to considerable production of soft X-rays by the electrons. These X-rays possess sufficient energy to cause photoemission of electrons from the anode. Electrically, the emission of an electron by the anode is equivalent to the capture of a positive ion, leading to a net excess current and thus to a lower limit for the detectable ion currents.

Having described the general set-up and the major components of a UHV system, some basic relations will be given, which can be used to calculate the performance and parameters of vacuum systems.

When a constant pressure p has been established in a UHV vessel, the number of molecules desorbing from the walls of the vessel must exactly balance the amount of gas being pumped away by the pumps. This is expressed by the so-called *pumping equation*, which relates the pressure change $\mathrm{d}p/\mathrm{d}t$ to the desorption rate v and the pumping speed $\tilde{S}$ [ℓ/s]. Since, for an ideal gas, volume and pressure are related by

$$pV = NkT, \tag{I.1}$$

the requirement of particle conservation yields

$$vA_\mathrm{v} = \frac{V_\mathrm{v}}{kT}\left(\frac{\mathrm{d}p}{\mathrm{d}t} + \frac{\tilde{S}p}{V_\mathrm{v}}\right), \tag{I.2}$$

where A_v and V_v are the inner surface area and the volume of the vacuum chamber, respectively. Stationary conditions are characterized in (I.2) by $\mathrm{d}p/\mathrm{d}t = 0$, whereas the pump-down behavior is found by solving (I.2) for $\mathrm{d}p/\mathrm{d}t$. Pumping speeds in vacuum systems are always limited by the finite conductance of the tubes through which the gas is pumped. The conductance C is defined as in Ohm's law for electricity by

$$I_\mathrm{mol} = C\Delta p/RT, \tag{I.3}$$

where I_mol is the molecular current, Δp the pressure difference along the tube and R the universal gas constant; C has the units ℓ/s as has the pumping speed $\tilde{S}$. In analogy with the electrical case (Kirchhoff's laws), two pipes in parallel have a conductance

$$C_\mathrm{p} = C_1 + C_2, \tag{I.4}$$

whereas two pipes in series must be described by a series conductance C_s satisfying

$$1/C_\mathrm{s} = 1/C_1 + 1/C_2. \tag{I.5}$$

Given that a certain pump is connected to a tube with a conductance C_p, the effective pumping speed $\tilde{S}_\mathrm{eff}$ of the pump is

$$1/\tilde{S}_\mathrm{eff} = 1/\tilde{S}_\mathrm{p} + 1/C_\mathrm{p} \tag{I.6}$$

where $\tilde{S}_\mathrm{p}$ is the pumping speed of the isolated pump without tube connection. The conductance of a pipe depends on the flow conditions, i.e. on the ratio between geometrical dimensions and mean free path of the molecules. For viscous flow ($pd > 10$ mbar mm) the conductance of a tube of circular cross section with diameter d and length L is obtained as

$$C[\ell/\mathrm{s}] = 137\frac{d^4[\mathrm{cm}^4]}{L[\mathrm{cm}]}p[\mathrm{mbar}]. \tag{I.7}$$

In the low-pressure regime of molecular flow ($pd < 0.1$ mbar mm) one has

$$C[\ell/\mathrm{s}] = 12\frac{d^3[\mathrm{cm}^3]}{L[\mathrm{cm}]}. \tag{I.8}$$

Further Reading

K. Diels, R. Jaeckel, *Leybold Vacuum Handbook* (Pergamon, London, 1966)
Leybold brochure, *Vacuum Technology—its Foundations, Formulae and Tables*, 9th edn., Cat. no. 19990 (1987)
J.F. O'Hanlon, *A Users' Guide to Vacuum Technology* (Wiley, New York, 1989)
J.P. Roth, *Vacuum Technology* (North-Holland, Amsterdam, 1982)
M. Wutz, H. Adam, W. Walcher, *Theorie and Praxis der Vakuumtechnik*, vol. 4 (Vieweg, Braunschweig, 1988)

Panel II
Basics of Particle Optics and Spectroscopy

Electrons and other charged particles such as ions are the most frequently used probes in surface scattering experiments (Chap. 4). The underlying reason is that these particles, in contrast to photons, do not penetrate deep into the solid. After scattering, they thus carry information about the top-most atomic layers of a solid. On the other hand, the fact that they are charged allows the construction of imaging and energy-dispersive equipment, e.g. monochromators for electrons, as used for photons in conventional optics. The basic law for the refraction (deflection) of an electron beam in an electric potential is analogous to Snell's law in optics. According to Fig. II.1, an electron beam incident at an angle a on a plate capacitor (consisting of two metallic grids) with applied voltage U is deflected. Due to the electric field $\mathcal{E}$ (normal to the capacitor plates) only the normal component of the velocity is changed from v_1 ($\perp$) to v_2 ($\perp$) the parallel component is unchanged, i.e.

$$\sin\alpha = \frac{v(\parallel)}{v_1}, \qquad \sin\beta = \frac{v(\parallel)}{v_2}, \tag{II.1a}$$

$$\frac{\sin\alpha}{\sin\beta} = \frac{v_2}{v_1} = \frac{n_2}{n_1}. \tag{II.1b}$$

This refraction law is analogous to the optical law if one identifies the velocity ratio with the ratio of refractive indices n_2/n_1. Assuming that the incident beam with velocity v_1 is produced by an accelerating voltage U_0, and that energy is conserved within the capacitor, i.e.,

$$\frac{m}{2}v_2^2 = \frac{m}{2}v_1^2 + eU, \tag{II.2}$$

one obtains the law of refraction

$$\frac{\sin\alpha}{\sin\beta} = \frac{v_2}{v_1} = \frac{n_2}{n_1} = \sqrt{1 + U/U_0}. \tag{II.3}$$

Inversion of the bias U_0 deflects the electron beam away from the normal. Describing the capacitor grids as equipotential surfaces for the field $\mathcal{E}$, the general description is that the electron beam is refracted towards or away from the normal to the

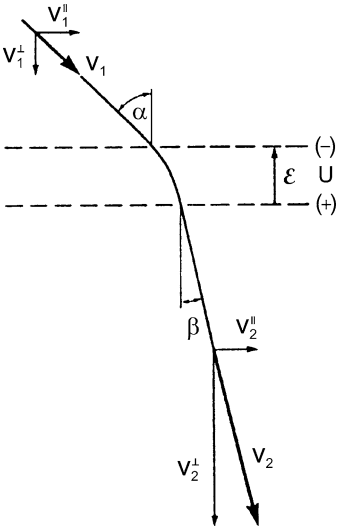

Fig. II.1 Classical electron trajectory through a parallel-plate capacitor. The electric field between the two transparent electrodes (*dashed lines*) changes the electron velocity component v_1 ($\perp$) into v_2 ($\perp$) but leaves the component $v(\parallel)$ unchanged

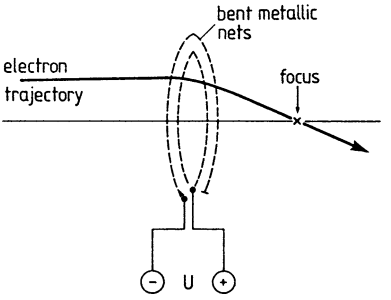

Fig. II.2 Simple model (optical analog) of an electron lens formed by two bent metallic grids which are biased by an applied voltage

equipotential lines depending on the gradient of the potential. In principle, (II.3) is also sufficient to construct, step by step, the trajectory of electrons moving in an inhomogenous electric field $\mathcal{E}(r)$. That is, of course, only true in the limit of classical particle motion, where interference effects due to the wave nature of the particle can be neglected (Sect. 4.9).

A simple but instructive model for an *electron lens* might thus appear as in Fig. II.2, in complete analogy to an optical lens. The metallic grid itself is not important, but rather the curvature of the non-material equipotential surfaces. Electron lenses can therefore be constructed in a simpler fashion, using metallic apertures which are themselves sufficient to cause curvature of the equipotential lines in their vicinity. The examples in Fig. II.3(a), (b) act as focussing and defocussing lenses because of their characteristic potential contours. The single lens in Fig. II.3(c) consists of three apertures arranged symmetrically in a region of constant ambient potential U_0. Although the field distribution in this lens is completely symmetric about the central plane with a saddle point of the potential in the center, the lens is always either focussing or, for extreme negative potentials at the center aperture, acts as an electron mirror. When the potential of the middle electrode is lower than that of

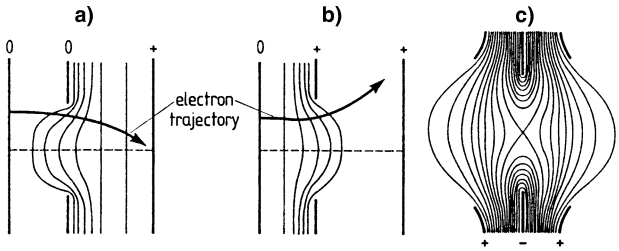

Fig. II.3 (**a**)–(**c**) Three examples of electron lenses formed by metallic apertures: (**a**) focussing arrangement, (**b**) defocussing arrangement, and (**c**) symmetrical single lens with focussing property. In each case characteristic equipotential lines are shown

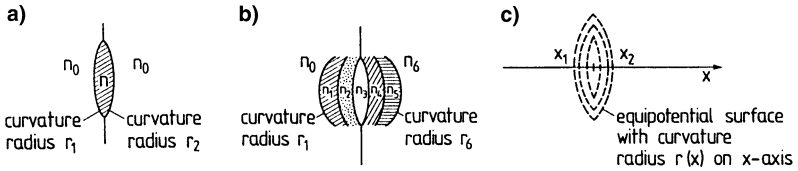

Fig. II.4 Comparison of the action of an electron lens formed by several different curved equipotential surfaces (**c**) with the optical analog, a single optical lens (refractive index n embedded in a medium with refractive index n_0) (**a**), and a multilayer lens consisting of differently curved layers with different refractive indices n_1 to n_5 embedded in two semi-infinite half spaces with refractive indices n_0 and n_6 (**b**)

the two outer electrodes, the speed of the electron decreases as it approaches the saddle point of the potential. The electron remains longer in this spatial range and the central region of the potential distribution has a more significant effect on the movement than do the outer parts. The central part of the potential, however, has a focussing effect, as one can see qualitatively by comparison with Fig. II.3(a), (b).

On the other hand, when the inner electrode is positive with respect to the outer electrodes, the electron velocity is lower in the outer regions of the lens, the declination to the central axis is dominant, and thus, in this case too, the lens has a focussing action.

For calculating the focal length f of an electrostatic lens we use the optical analog (Fig. II.4). A simple focussing lens with two different radii of curvature embedded in a homogeneous medium of refraction index n_0 has an inverse focal length of

$$\frac{1}{f} = \frac{n - n_0}{n_0}\left(\frac{1}{|r_1|} + \frac{1}{|r_2|}\right) = \frac{\Delta n}{n_0}\left(\frac{1}{r_1} - \frac{1}{r_2}\right). \tag{II.4}$$

The formula for a layered lens system, as shown in Fig. II.4(b), is obtained by simple generalization as

$$\frac{1}{f} = \frac{1}{n_0}\sum_{v=1}^{5}\frac{\Delta n_v}{r_v}, \quad v = 1, 2, 3, 4, 5. \tag{II.5}$$

The formulae are, of course, only correct for trajectories close to the axis. The focal length for an electron lens with equipotential lens as in Fig. II.4(c) is obtained by analogy as

$$\frac{1}{f} = \frac{1}{n_2}\int_{n_1}^{n_2}\frac{\mathrm{d}n}{r(x)} = \frac{1}{n_2}\int_{x_1}^{x_2}\frac{1}{r(x)}\frac{\mathrm{d}n}{\mathrm{d}x}\mathrm{d}x, \tag{II.6}$$

where $r(x)$ and $n(x)$ are the radius of curvature and the "electron refractive index" according to (II.3) at a point x on the central axis. The field distribution extends from x_1 to x_2 on the axis. The refractive index for electrons (II.3) depends on the square root of the potential $U(x)$ on the axis and the electron velocity $v(x)$ as

$$n(x) = \frac{v(x)}{v_1} = \text{const}\frac{[U(x)]^{1/2}}{v_1}. \tag{II.7}$$

For electron trajectories close to the axis one therefore obtains an inverse focal length of

$$\begin{aligned}\frac{1}{f} &= \frac{v_1}{\text{const}\ (U_2)^{1/2}}\int_{x_1}^{x_2}\frac{1}{r(x)}\frac{\frac{1}{2}\text{const}\ U'(x)/v_1}{[U(x)]^{1/2}}\mathrm{d}x \\ &= \frac{1}{2(U_2)^{1/2}}\int_{x_1}^{x_2}\frac{1}{r(x)}\frac{U'(x)}{[U(x)]^{1/2}}\mathrm{d}x.\end{aligned} \tag{II.8}$$

Apart from boundary conditions (boundary potentials U_2, U_1) the focal length f results as a line integral over an expression containing $[U(x)]^{1/2}$ and $U'(x)$, the first derivative of the potential.

Since the charge/mass ratio e/m does not enter the focussing conditions, not only electrons but also positive particles such as protons, He^+ ions, etc. are focussed at the same point with the same applied potentials, provided they enter the system with the same geometry and the same primary kinetic energy.

This is not the case for magnetic lenses, which are used mainly to focus high energy particles. For electrons, the focussing effect of a magnetic field is easily seen for the example of a long solenoid with a nearly homogeneous magnetic field in the interior (Fig. II.5).

An electron entering such a solenoid (with velocity v) at an angle φ with respect to the B field, is forced into a helical trajectory around the field lines. This motion is described by a superposition of two velocity components $v_\parallel = v\cos\varphi$ and $v_\perp = v\sin\varphi$, parallel and normal to the B field. Parallel to B there is an unaccelerated motion with constant velocity $v_\parallel$; normal to B the particle moves on a circle with angular frequency

$$\omega = \frac{2\pi}{\tau} = \frac{e}{m}B, \tag{II.9}$$

i.e., the time $\tau = 2\pi m/eB$ after which the electron recrosses the same field line is not dependent on the inclination angle φ. All particles entering the solenoid at

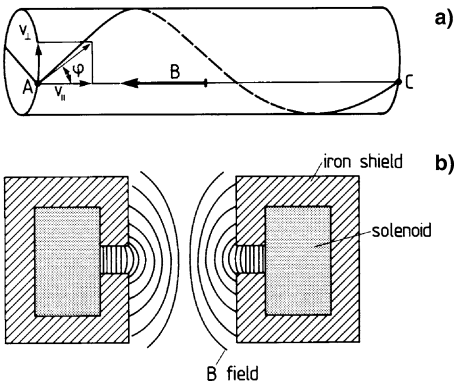

Fig. II.5 Magnetic lens for electrons. (**a**) Schematic explanation of the focussing action. An electron entering a "long" solenoid adopts a helical trajectory around the magnetic field B such that after a certain time, τ, it recrosses the same B-field line through which it entered (points A and C). (**b**) Practical form of a magnetic lens consisting of a short ion-shielded solenoid

point A at different angles reach the point C after the same time T. Particles originating from A are thus focussed at C. The distance AC is given by the parallel velocity $v_\parallel$ and the time τ as

$$\mathrm{AC} = v_\parallel \tau = \frac{2\pi m v \cos\varphi}{eB}. \tag{II.10}$$

For a magnetic lens the focussing condition is thus dependent on e/m, i.e. on the charge and mass of the particles. Furthermore the image is tilted in relation to the object due to the helical motion of the imaging particles. Practical forms of the magnetic lens are sometimes constructed by means of short iron-shielded solenoids with compact, concentrated field distributions in the interior (Fig. II.5(b)).

Also important in surface physics, in addition to the construction of imaging electron optics in electron microscopes, scanning probes, etc. (Panel V: Chap. 3), is the availability of dispersive instruments for energy analysis of particle beams. The main principles of an electrostatic electron energy analyzer are discussed in the following.

This type of analyzer has as its main components two cylinder sectors as electrodes and is thus called a *cylindrical analyzer* (Fig. II.6). A well-defined pass energy E_0 for electrons on a central circular path between the electrodes is defined by the balance between centrifugal force and the electrostatic force of the field $\mathcal{E}$ due to the voltage U_p applied across the electrodes. The field is a logarithmic radial field:

$$\mathcal{E} = -\frac{U_\mathrm{p}}{r \ln(b/a)} \tag{II.11}$$

with a and b as the inner and outer radii of the region between the cylindrical sectors (Fig. II.6); r is the radius vector to an arbitrary point of the field, whereas r_0 and v_0 are the radius vector and tangential velocity on the central trajectory, i.e. they satisfy

$$\frac{m v_0^2}{r_0} = -e\mathcal{E}_0 = \frac{eU_\mathrm{p}}{r_0 \ln(b/a)}. \tag{II.12}$$

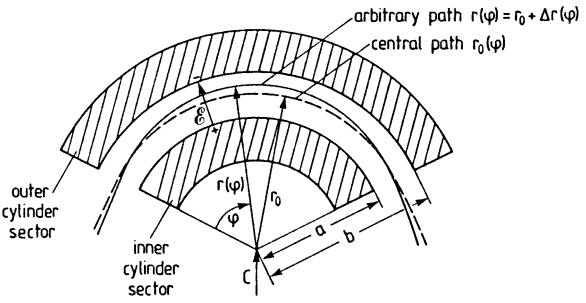

Fig. II.6 Electrostatic cylinder sector energy analyzer (schematic). The electric field between the two cylinder sectors (shaded) exactly balances the centrifugal force for an electron on the central path r_0. An arbitrary electron path around the central path is described by the deviation $\Delta r(\varphi)$ from the central path

The pass energy is thus obtained as

$$E_0 = \frac{1}{2} m v_0^2 = \frac{1}{2} \frac{e U_\mathrm{p}}{\ln(b/a)}. \tag{II.13}$$

Under certain conditions such a cylindrical analyzer has additional focussing properties, which considerably enhance its transmittance and are thus advantageous for investigations with low beam intensities. This can be seen by considering an electron path inclined at a small angle α to the central path at the entrance (Fig. II.6). This path is described by the dynamic equation.

$$m \frac{\mathrm{d}^2 r}{\mathrm{d}t^2} = m \frac{v^2}{r} - e\mathcal{E} = m r \omega^2 - e\mathcal{E}, \tag{II.14}$$

where ω is the angular velocity around the center C. For small deviations from the central path r_0 one has

$$r \simeq r_0 + \Delta r, \tag{II.15a}$$

$$\mathcal{E} \simeq \mathcal{E}_0 r_0 / r = \mathcal{E}_0 (1 - \Delta r / r_0). \tag{II.15b}$$

The angular momentum around C must be conserved, i.e., neglecting small quantities we have

$$\omega r^2 \simeq \omega_0 r_0^2. \tag{II.16}$$

From (II.14)–(II.16) one obtains the approximate dynamic equation

$$\frac{\mathrm{d}^2 r}{\mathrm{d}t^2} = \frac{\omega_0^2 r_0^4}{r^3} - \frac{e\mathcal{E}}{m}, \tag{II.17}$$

or

$$\frac{\mathrm{d}^2(\Delta r)}{\mathrm{d}t^2} = \omega_0^2 \frac{r_0^4}{(r_0 + \Delta r)^3} - \frac{e}{m} \mathcal{E}_0 \left(1 - \frac{\Delta r}{r_0}\right). \tag{II.18}$$

Using (II.12) and neglecting small quantities in second order yields

$$\frac{d^2(\Delta r)}{dt^2} + 2\omega_0^2 \Delta r = 0. \tag{II.19}$$

The solution for the deviation Δr from the central path is thus obtained as

$$\Delta r = \text{const} \times \sin(\sqrt{2}\omega_0 t + \delta), \tag{II.20}$$

i.e. the deviation oscillates with a period $(2)^{1/2}\omega_0$. An electron entering the analyzer on the central path ($\delta = 0$) crosses that path again after a rotation angle $\phi = \omega_0 t$ (around C), which is given by

$$\sqrt{2}\omega_0 t = \sqrt{2}\phi = \pi, \tag{II.21a}$$

or

$$\phi = 127^\circ\ 17'. \tag{II.21b}$$

This is independent of α, i.e. focussing occurs for cylindrical sectors with an angle of $127^\circ\ 17'$. In reality the electric field $\mathcal{E}$ is perturbed at the entrance and at the exit of the analyzer. A field correction is performed by so-called *Herzog apertures* which define the entrance and exit slits. This modifies the condition (II.21a), (II.21b) and leads to a sector angle for focussing of 118.6°. For judging the performance of such analyzers the energy resolution $\Delta E/E$ is an important quantity. From an approximate, more general solution for the electron trajectories one obtains

$$\frac{\Delta E}{E} = \frac{x_1 + x_2}{r_0} + \frac{4}{3}\alpha^2 + \beta^2, \tag{II.22}$$

where x_1 and x_2 are the width and length of the rectangular entrance (and exit) slits, and α and β are the maximum angular deviations of the electron trajectories at the entrance, in the plane and normal to the plane of Fig. II.6. Present-day instruments employed in electron scattering experiments (HREELS, Panel X: Chap. 4) achieve a resolution $\Delta E/E$ of 10^{-3}–10^{-4}. Decreasing the slit width to improve the resolution is only possible within certain limits, since it simultaneously reduces the transmitted current. This deterioration is mainly due to space-charge effects. Electrons moving parallel to one another through the analyzer interact with each other via their Coulomb repulsion and their mutually induced magnetic field (due to the current). For high electron densities these space-charge effects distort the electron trajectories and limit the resolution. A semi-quantitative estimate of the effect can be made using the classical formula for space-charge-limited currents in radio tubes:

$$j \propto U^{3/2}. \tag{II.23}$$

Using (II.22) one therefore obtains for the current density at the entrance

$$j_i \propto E_0^{3/2} \propto (\Delta E)^{3/2}. \tag{II.24}$$

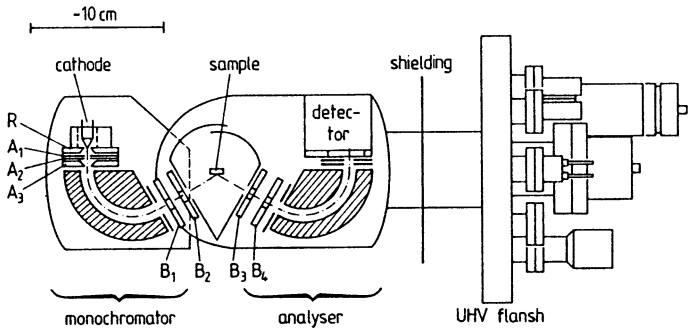

Fig. II.7 Schematic plot of a high-resolution electron energy loss spectrometer consisting of a cathode system (filament with lens system), a monochromator (cylindrical sectors), a similar analyzer and a detector. The monochromator can be rotated around an axis through the sample surface. The whole set up is mounted on a UHV flange

The final current density at the exit, then follows as

$$j_f \propto j_i \Delta E \propto (\Delta E)^{5/2}. \tag{II.25}$$

This dependence, which is confirmed well by experiment, causes a strong reduction of the transmitted current with narrower entrance slits.

Electron analyzers can be used in two modes: Scanning the pass voltage U_p by an external ramp varies the passing energy E_0 (II.13). Because of (II.22) the ratio $\Delta E/E$ remains the same, i.e. when the pass energy is varied, the resolution ΔE also changes continuously across the spectrum (constant $\Delta E/E$ mode). In order to achieve a constant resolution over the entire spectrum, the pass energy of the analyzer and thus also the resolution ΔE can be held constant; but the electron spectrum being measured, must then be "shifted" through the fixed analyzer window ΔE by variation of an acceleration or deceleration voltage in front of the analyzer (constant ΔE mode).

A complete electron spectrometer (Fig. II.7) such as those used for High-Resolution Electron Energy Loss Spectroscopy (HREELS, Sect. 4.6) consists of at least two analyzers with focussing apertures (lenses) at the entrances and exits. A cathode arrangement with a lens system produces an electron beam with an energetic halfwidth of 0.3–0.5 eV (Maxwell distribution of hot electrons). The first electron monochromator (the same as the analyzer) is fixed at a constant pass energy and selects electrons in an energy window of width 1–10 meV from the broad Maxwell distribution. This primary beam is focussed onto the crystal surface by a lens system. The voltage applied between this lens and the sample determines the primary energy. The backscattered electrons are focussed by a second lens system onto the entrance slit of the second analyzer which is usually used in the constant ΔE mode, i.e. with a fixed pass energy and a variable acceleration voltage between sample and analyzer. A lens system behind the exit slit focusses the analyzer beam onto a detector, a Faraday cup or, more often, a channeltron electron multiplier.

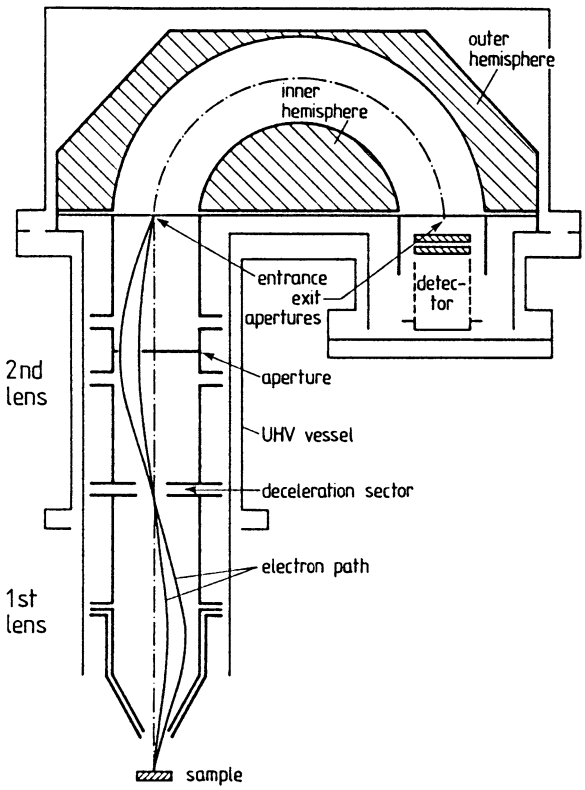

Fig. II.8 Schematic plot of a hemispherical electron energy analyzer consisting of two entrance lenses which focus the incoming electrons onto the entrance aperture, two hemispherical electrodes facilitating energy analysis and a detector (e.g., secondary-electron multiplier)

In addition to the cylindrical electron analyzer discussed so far, a number of other electrostatic analyzers are in use. Similar in its principles is the so-called *hemispherical analyzer* (Fig. II.8) in which the electric field balancing the centrifugal force of the electrons on their trajectory is formed between two metallic hemispheres. Entrance and exit apertures are circular holes, which also produce a circular image, in contrast to the rectangular image of the cylindrical analyzer. In common with the latter, a focussing condition exists for electrons that have been deflected through an angle of 180°. Thus the hemispherical shape of the electrodes is an essential requirement for focussing. The energy resolution is calculated as

$$\frac{\Delta E}{E} = \frac{x_1 + x_2}{2\overline{r}} + \alpha^2, \quad \overline{r} = \frac{a+b}{2}, \tag{II.26}$$

where x_1 and x_2 are the radii of the entrance and exit apertures, and a and b are the radii of the inner and outer spheres; α is the maximum angular deviation of the electron trajectories at the entrance with respect to the center line (normal to entrance aperture). Lens systems such as that shown in Fig. II.8 are also used in combination with this type of analyzer.

A widely used analyzer, in particular for Auger Electron Spectroscopy (AES), is the so-called *Cylindrical Mirror Analyzer* (CMA). Here the electrons entering from

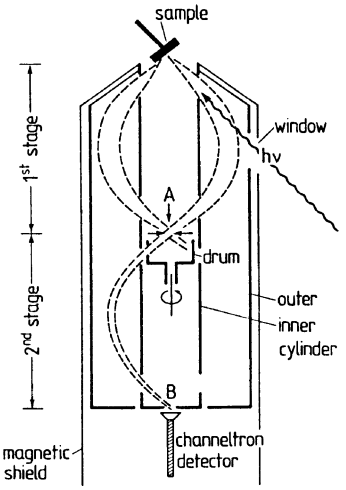

Fig. II.9 Double stage Cylindrical Mirror Analyzer (CMA) consisting of two analyzer units. For photoemission experiments the exciting light beam enters through a window and hits the sample surface. The emitted electrons enter the analyzer (outer and inner cylindrical mirror) within a certain cone. Measurements with angular resolution can be performed by means of a rotatable drum in front of the entrance to the second stage. A window in the drum selects electrons from one particular direction only. The second stage images point A into point B at the channeltron detector

an entrance point into a certain cone are focussed by two concentric, cylindrical electrodes onto an image point, where the detector (e.g., a channeltron) is positioned. One also encounters double-stage CMAs with two successive analyzer units (Fig. II.9). The electric field determining the pass energy is a radial field between the two concentric electrodes. Focussing occurs for electrons entering near a cone with an apex angle $\phi = 42^\circ\ 18.5'$ (Fig. II.9). This acceptance cone and the total acceptance aperture (circle) around the cone are determined by appropriate windows in the cylindrical electrodes. The pass energy E_0 and pass voltage U_p between the two cylinders are related by

$$E_0 = \frac{eU_\mathrm{p}}{0.77\ln(b/a)}. \tag{II.27}$$

The energy resolution of this CMA is determined both by the angular deviation α of the incoming electron trajectory from the well-defined acceptance cone and by the axial shifts x_1 and x_2 of the actual electron trajectories with respect to the ideal entrance and image points on the cylinder axis (Fig. II.9). An approximate numerical calculation yields:

$$\frac{\Delta l}{l_0} = \frac{x_1 + x_2}{l_0} = \frac{\Delta E}{E}(1 + 1.84\alpha) - 2.85\alpha^2. \tag{II.28}$$

Finally, we mention briefly the electronic circuitry common to the control units of all these electrostatic analyzers. It is always necessary to scan the potential V_0 at the

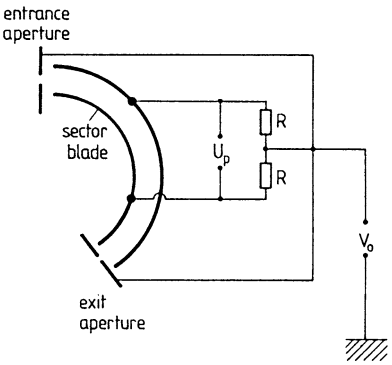

Fig. II.10 Simple electronic circuit for supplying the appropriate voltages to an electron energy analyzer

entrance and exit slits, which is identical to the potential of the central path within the analyzer. Simultaneously the potentials on the two main electrodes (cylinder sectors, hemispheres, etc.) must remain symmetrically disposed with respect to the potential on the central path when the pass voltage U_p is varied. This is achieved by means of a circuit such as that shown schematically in Fig. II.10.

Besides the types of analyzer described above, retarding field analyzers are also in use. In principle, these are high-pass filters in which a variation of the retarding voltage determines a variable cut-off kinetic energy for the electrons. These retarding field analyzers can simultaneously be used as optical LEED display units in electron diffraction experiments. A detailed description is given in Panel VIII: Chap. 4.

Further Reading

P. Grivet, *Electron Optics* (Pergamon, Oxford, 1965)
H. Ibach, *Electron Energy Loss Spectrometers*. Springer Ser. Opt. Sci., vol. 63 (Springer, Berlin, 1990)

Problems

Problem 1.1 A spherical UHV chamber with a volume of 0.5 m^3 is pumped through a circular tube with a diameter of 20 cm and a length of 50 cm. The used sputter ion pump has a pumping speed of 1000 ℓ/s. The end pressure reached after baking out the vessel is $7 \cdot 10^{-11}$ Torr. What is the gas desorption rate from the walls of the UHV chamber at steady state?

Problem 1.2 In the low-pressure regime of molecular flow the molecules do not hit each other, they are only reflected from the walls of the tube. The molecular flow through a tube of diameter d and length L might thus be described roughly by a diffusion process in which the mean-free path is approximated by the tube diameter and the gradient of the particle density along the tube by $\mathrm{d}n/\mathrm{d}x = \Delta n/L$. Using the standard formulae for current density, diffusion coefficient, etc., derive the conductance equation (I.8) for molecular flow: $C \propto d^3/L$.

Problem 1.3 An electron beam is accelerated by a voltage of 500 V and penetrates an arrangement of two parallel metallic grids under an angle of 45° toward the grid plane. Between the grids a bias of 500 V is applied (minus at first, plus at second grid). Under what angle, with respect to the grid normal, is the electron beam detected behind the grid arrangement. What is the kinetic energy of the electrons behind the grids?

Problem 1.4 An electron penetrates a short region of varying potential $U(x)$. Calculate the curvature radius of its trajectory from the acting centripetal force.

http://www.springer.com/978-3-319-10755-4

Solid Surfaces, Interfaces and Thin Films

Lüth, H.

2015, XIII, 589 p. 443 illus., 21 illus. in color., Hardcover
ISBN: 978-3-319-10755-4